Nano Research

Open Access

Research Article

Monodisperse metal-organic cages for gas chromatographic separation

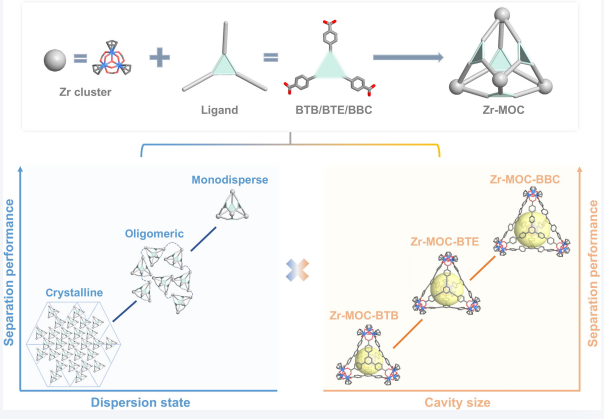
Sha-Sha Meng[§], Cheng-Yu Rong[§], Ming Xu ✉, and Zhi-Yuan Gu

State Key Laboratory of Microbial Technology, Jiangsu Key Laboratory of Biofunctional Materials, Jiangsu Collaborative Innovation Center of Biomedical Functional Materials, Jiangsu Key Laboratory of New Power Batteries, Jiangsu Key Laboratory of Micro-Nano Sensing and Separation Science for Analytical Chemistry, College of Chemistry and Materials Science, School of Food Science and Pharmaceutical Engineering, Nanjing Normal University, Nanjing 210023, China

[§] *Sha-Sha Meng and Cheng-Yu Rong contributed equally to this work.*

Cite this article: *Nano Research*, **2026**, *19*, 94908924. https://doi.org/10.26599/NR.2026.94908924

ABSTRACT: Establishing the definitive structure–performance relationship in metal-organic cage (MOC) stationary phases requires isolating intrinsic cavity contributions from dispersion-induced artifacts. However, solvent-dependent dispersion behavior of MOCs often obscures the direct role of molecular cage architecture in chromatographic separation. Here, we constructed a structurally homologous series of Zr-based MOCs with identical V_4F_4 topology but systematically enlarged cavity and window sizes through ligand elongation, including two newly constructed cages. Systematic investigation of solvent-dependent behavior revealed distinct states ranging from crystalline assemblies to oligomeric aggregates and ultimately to monodisperse cages. When utilized as gas chromatographic (GC) stationary phases, only monodisperse Zr-MOCs translated their discrete cage architectures into efficient separations, establishing dispersion control as a prerequisite for accessing intrinsic structure–property relationships. Under monodisperse conditions, Zr-MOC-BBC (BBC = 1,3,5-tris(4'-carboxy[1,1'-biphenyl]-4-yl)benzene) with the largest cavity exhibited the highest separation resolution compared to Zr-MOC-BTB (BTB = 1,3,5-tris(4-carboxyphenyl)-benzene) and Zr-MOC-BTE (BTE = 4,4',4''-(benzene-1,3,5-triyltris(ethyne-2,1-diyl))tribenzoic acid). Mechanistic analysis demonstrated that the dispersion state primarily governed diffusion-controlled mass transfer, whereas intrinsic cavity size influenced both mass transfer resistance and thermodynamic host–guest interactions. This work demonstrates that controlling dispersion state is essential for accessing the intrinsic cavity and provides insights into the design of MOC-based separation materials.



KEYWORDS: metal-organic cage, monodisperse state, cavity architecture, chromatographic separation

1 Introduction

Metal-organic cages (MOCs) [1–5], as an emerging class of supramolecular materials, are constructed through coordination-driven self-assembly of metal clusters or ions with organic ligands. Their well-defined cage-like structures, intrinsic porosity, and tunable cavities endow them with nanoscale dimensions [6, 7], structural versatility [8–10], and excellent solution processability [11–15]. These characteristics make MOCs promising candidates for gas chromatographic (GC) stationary phases. However, translating MOCs from molecular constructs into practical GC stationary phases faces a long-overlooked challenge that the separation function of their intrinsic cage cavities is often neglected. Typically, MOCs exhibit pronounced solvent-dependent dispersion behaviors, ranging from monodisperse cages to oligomeric assemblies or crystalline packing under different solvents [11, 16–18]. In non-ideal dispersion states, partial inter-cage association or dense packing can significantly restrict the accessibility of intrinsic cavities, while simultaneously introducing transport pathways dominated by interstitial stacking voids rather than cage interiors. Under such conditions, chromatographic behavior is significantly governed by extrinsic packing effects,

Received: April 7, 2026; **Revised:** June 1, 2026
Accepted: June 8, 2026

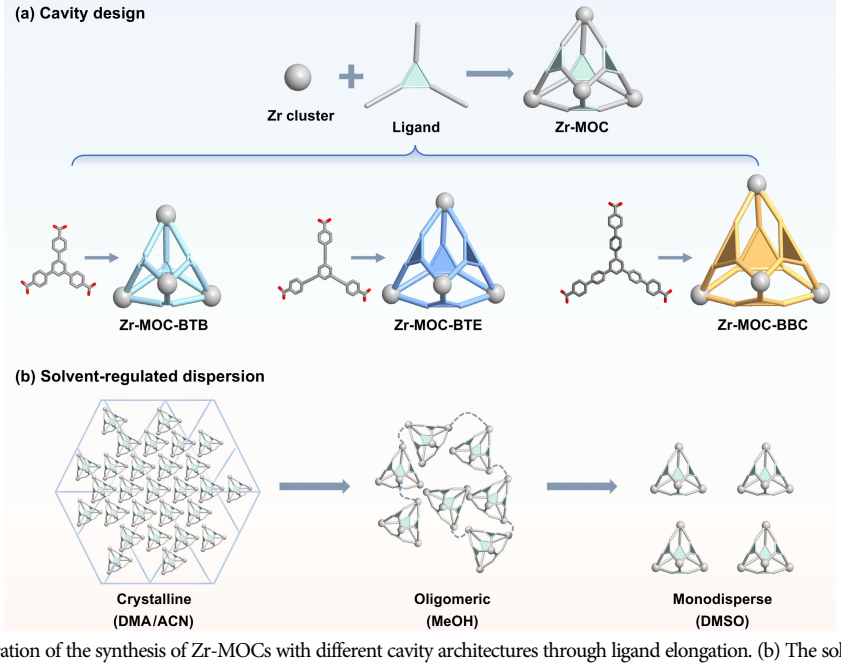
✉Address correspondence to mingxu@njnu.edu.cn

making it difficult to establish the definitive structure–performance relationship between intrinsic cage architecture and separation performance.

Previous studies have demonstrated the feasibility of MOCs as GC stationary phases, particularly in chiral separations [19, 20]. However, these studies typically involved materials with varying dispersion states, where the observed separation performance was not necessarily dominated by the inherent cavities of the cages themselves. For example, Yuan et al. reported the first chiral MOC ($[Zn_3L_2]$) [21] coated column for the separation of position isomers, polycyclic aromatic hydrocarbons, and racemates, followed by related systems such as $[Fe_4L_6](ClO_4)_8$ [22], $[Cu_{12}(L_V)_{12}(H_2O)_{12}]$ [23], MOC-PA [24], and tetrahedral cage $Fe^{II}_4L_4$ [25]. In most cases, polymeric binders or auxiliary stationary phases that inherently possessed non-chiral separation capability were introduced to facilitate coating. The reported separation performance often arose from synergistic contributions of these components and MOCs. These studies primarily highlighted the potential of MOCs for host–guest recognition by emphasizing their chiral microenvironments, without explicitly addressing whether analytes traverse the intrinsic cage cavities, as surface-accessible interaction sites alone were often sufficient to achieve separation. Even in systems using pure MOCs, the recognition was largely remained on chiral recognition sites, while the dispersion state of the cages was still overlooked, rendering it unclear whether the intrinsic cavities actively contributed to the separation process [24].

Recent studies on porous coordination materials have highlighted the importance of establishing structure–performance relationships between pore architecture and separation behavior [26–30]. Elucidating the intrinsic role of cage cavities in governing separation behavior is essential for guiding the rational design of high-performance MOC-based stationary phases, yet this remains a significant challenge. First, it requires maintaining MOCs in a monodisperse state while avoiding the introduction of extrinsic components that could contribute additional separation effects. Second, the cage structures themselves must possess inherent separation capability, rather than only relying on external interactions. Third, both the cage architecture and its associated separation performance should be tunable, enabling systematic correlation between structural parameters and separation behavior, and thereby allowing the establishment of general design principles centered on intrinsic cavity functionality.

Herein, we report two newly constructed Zr-based MOCs, Zr-MOC-BTE (BTE = 4,4',4''-(benzene-1,3,5-triyltris(ethyne-2,1-diyl))tribenzoic acid) and Zr-MOC-BBC (BBC = 1,3,5-tris(4'-carboxy[1,1'-biphenyl]-4-yl)benzene), alongside the previously reported Zr-MOC-BTB (BTB = 1,3,5-tris(4-carboxyphenyl)-benzene) [31]. All three MOCs exhibited the same V_4F_4 tetrahedral topology, while their cavity and window size were systematically tuned through ligand elongation (Scheme 1). This homologous structural series enabled controlled modulation of intrinsic geometric parameters without altering overall topology. Solvent-dependent dispersion studies identified conditions under which these Zr-MOCs could be stabilized in a monodisperse state, enabling a clear distinction between dispersion effects and intrinsic cavity contributions. Because the stable dispersed state was formed only after solvent removal upon heating, no additional separation-contributing factors were introduced. By establishing comparable monodisperse stationary phases, we demonstrated that chromatographic performance was governed first by dispersion state. Oligomerization induced inter-cage packing, generating irregular stacking voids that led to disordered diffusion pathways and increased mass transfer resistance, thereby aggravating peak broadening and reducing separation resolution. In contrast, under monodisperse conditions, the cages exhibited enhanced separation capability. Once monodispersity was ensured, the separation performance of the cages was further modulated by their intrinsic cavity size. In particular, Zr-MOC-BBC, with the largest cavity, exhibited the highest separation resolution. Mechanistic investigation indicated that cavity enlargement simultaneously attenuated mass-transfer resistance and modulated enthalpy–entropy contributions to retention, thereby directly



Scheme 1 (a) Schematic illustration of the synthesis of Zr-MOCs with different cavity architectures through ligand elongation. (b) The solvent-regulated dispersion states of Zr-MOCs.

translating molecular geometry into macroscopic separation performance. This work establishes a direct link between intrinsic cage architecture and GC separation behavior, providing a conceptual framework for rational design of next-generation MOC-based stationary phases.

2 Results and discussion

2.1 Design and structural characterization of Zr-MOCs with tunable cavity architectures

To systematically investigate the influence of intrinsic cage cavities on chromatographic separation, a homologous series of Zr-MOCs with identical topology but progressively enlarged internal cavities was designed and synthesized. By elongating the tricarboxylate ligands from H_3BTB to H_3BTE and H_3BBC, Zr-MOC-BTB, Zr-MOC-BTE, and Zr-MOC-BBC were obtained under comparable solvothermal conditions using zirconocene dichloride (Cp_2ZrCl_2) as the metal precursor. As illustrated in Fig. 1, all three Zr-MOCs shared the same V_4F_4 tetrahedral topology, in which four trinuclear $[Cp_3Zr_3(\mu_3\text{-}O)(\mu_2\text{-}OH)_3]$ clusters occupied the vertices and four organic ligands spanned the faces of the cage. Importantly, systematic elongation of the organic ligand backbone led to a continuous expansion of the internal cavity and window apertures, while preserving the overall cage connectivity. Specifically, the internal cavity diameters expanded from 0.82 nm for Zr-MOC-BTB to 1.06 nm for Zr-MOC-BTE and 1.20 nm for Zr-MOC-BBC, accompanied by an increase in window sizes from 0.42 to 0.64 and 0.76 nm (Figs. 1(b) and 1(c)). This design strategy enables modulation of intrinsic pore architecture without altering the coordination topology, providing a structurally well-defined platform for probing cavity-dependent separation behavior.

Zr-MOC-BTB packed and crystallized as octahedral crystals, consistent with previous reports (Fig. S1 in the Electronic Supplementary Material (ESM)) [31]. Zr-MOC-BTE and Zr-MOC-BBC, synthesized for the first time, exhibited hollow rod-like crystals and microcrystalline particles, respectively. The scanning electron microscopy (SEM) images further confirmed the microrod morphology of Zr-MOC-BBC (Fig. S2 in the ESM). Powder X-ray diffraction (PXRD) patterns of as-synthesized Zr-MOC-BTB were in good agreement with the simulated profile, confirming its high crystallinity and the expected V_4F_4 topology (Fig. 2(a)). In comparison, the PXRD patterns of as-synthesized Zr-MOC-BTE and Zr-MOC-BBC also exhibited well-defined diffraction peaks, indicating that both MOCs were highly crystalline (Fig. 2). Due to the limited quality of single-crystal diffraction data for Zr-MOC-BTE and the unsuitable crystal size of Zr-MOC-BBC, their structures were analyzed by the Pawley refinement against the simulated V_4F_4 model derived from Zr-MOC-BTB (Figs. 2(b) and 2(c)). The low residual values obtained from refinements indicated excellent agreement between the experimental and simulated profiles (Table S1 in the ESM), confirming that ligand elongation did not alter the underlying cage topology.

The thermal stability of the as-synthesized Zr-MOCs was evaluated by the thermogravimetric analysis (Fig. 2(d)). All as-synthesized Zr-MOCs showed initial weight loss below 200 °C, attributable to the removal of residual solvents, followed by framework decomposition above 400 °C. The similar thermal profiles indicated that ligand elongation did not compromise the thermal stability of the Zr-MOCs, supporting the structural integrity of the discrete cages after the solvent removal. The decomposition temperatures above 400 °C further demonstrated that these Zr-MOCs possessed sufficient thermal stability to withstand the high-temperature thermal conditioning and GC separation processes.

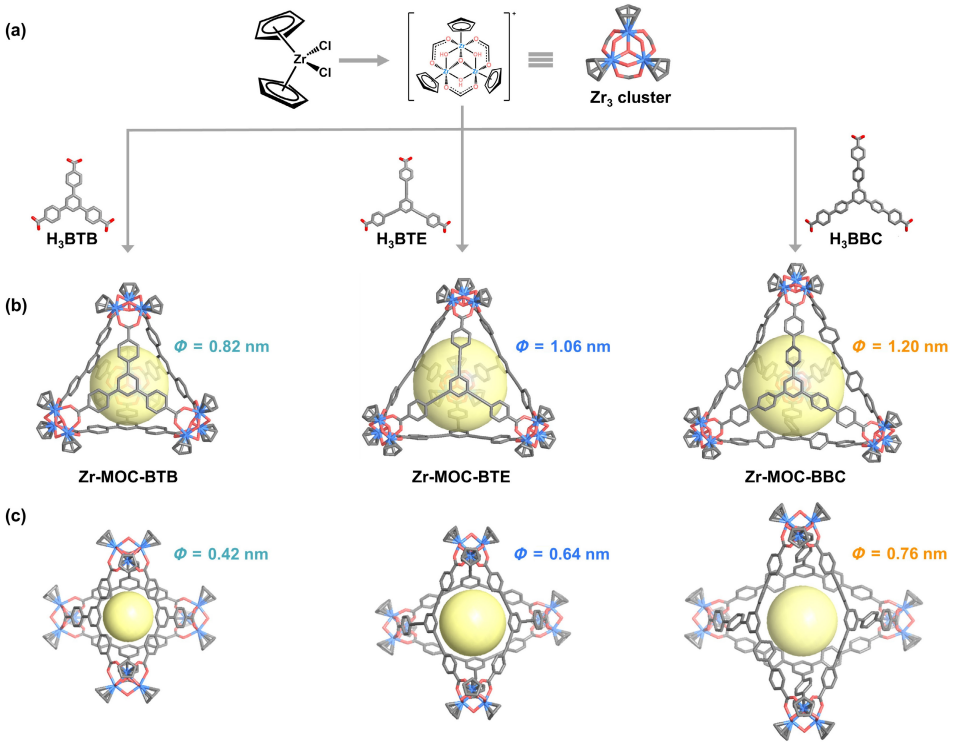


Figure 1 (a) The synthesis of Zr-MOC-BTB, Zr-MOC-BTE, and Zr-MOC-BBC through coordination of Zr clusters with H_3BTB, H_3BTE, and H_3BBC ligands, respectively. ((b) and (c)) The simulated (b) cavity size and (c) window size of Zr-MOC-BTB, Zr-MOC-BTE, and Zr-MOC-BBC, respectively.

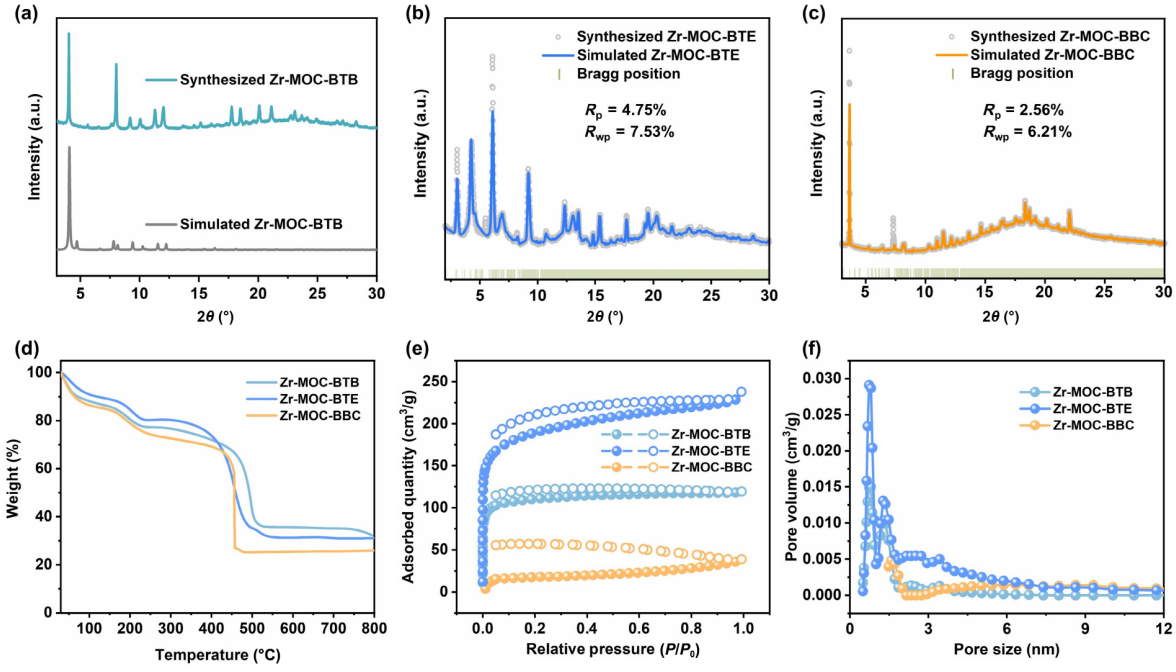


Figure 2 (a) The PXRD patterns of as-synthesized Zr-MOC-BTB and the corresponding simulated one. ((b) and (c)) Pawley refinement of Zr-MOC-BTE and Zr-MOC-BBC. The experimental and calculated curves were in blue and gray, respectively. The vertical bars indicated the positions of the Bragg peaks. (d) TGA plots of Zr-MOCs. (e) N_2 adsorption–desorption isotherms of Zr-MOCs measured at 77 K. (f) Pore size distributions calculated from the DFT method.

The permanent porosity of Zr-MOCs was evaluated by N_2 adsorption–desorption measurements at 77 K. Prior to the measurements, all Zr-MOCs were activated under vacuum at 40 °C for 12 h (see the ESM for detail). Thermo gravimetric analysis (TGA) curves of the activated samples indicated that a small amount of residual solvent remained after activation under this mild condition (Fig. S3 in the ESM). The higher activation temperatures led to almost no residual solvent but a nearly complete loss of N_2 adsorption capacity (Fig. S4 in the ESM), suggesting loss of accessible intermolecular voids induced by excessive desolvation. Therefore, the mild activation at 40 °C was employed to preserve the accessible porous structure of the Zr-MOCs. All three Zr-MOCs exhibited Type I isotherms (Fig. 2(e)), indicating the characteristic of micropores. The maximum adsorption capacities of Zr-MOC-BTB, Zr-MOC-BTE, and Zr-MOC-BBC were 119, 238, and 39 cm^3/g, respectively. Correspondingly, the Brunauer–Emmett–Teller (BET) surface areas were determined to 417, 696, and 58 m^2/g, respectively (Table S2 in the ESM). A clear porosity hierarchy of Zr-MOC-BTE > Zr-MOC-BTB > Zr-MOC-BBC was observed in both N_2 uptake and BET surface area, which was inconsistent with the expected trend based on the predefined cage size sequence. This trend reflected the combined influence of intrinsic cavity size and solid-state packing effects. Ligand elongation from BTB to BTE can increase the internal cavity volume while preserving the packing characteristic, leading to enhanced accessible microporosity in Zr-MOC-BTE. In contrast, despite possessing a theoretically large intrinsic cavity, Zr-MOC-BBC exhibited markedly lower porosity. This discrepancy likely arose from packing disorder or partial structural disruption during activation, which may reduce the accessibility of the cage cavities [32–35]. For Zr-MOC-BTB and Zr-MOC-BTE, the pore size distributions calculated from the density functional theory (DFT) method were similar, both featuring a dominant peak centered at approximately 0.80 nm (Fig. 2(f)), corresponding to the intrinsic tetrahedral cage cavity. Additional peaks at 1.27 nm and within the range of 2–4 nm were attributed to interstitial voids generated by inter-cage packing [36]. The nearly identical pore size profiles indicated that both MOCs largely retained their intrinsic architectures upon activation, with Zr-MOC-BTE providing increased pore volume due to its expanded cavity size. Nevertheless, Zr-MOC-BBC showed a primary intrinsic pore around 1.60 nm, accompanied by a broad distribution of stacking-induced pores (Fig. S5 in the ESM). The extensive presence of irregular inter-cage voids, together with pronounced desorption hysteresis, implied structural heterogeneity and disordered aggregation during activation.

After activation, the diffraction peaks of Zr-MOCs became significantly broadened or largely disappeared (Fig. S6 in the ESM), indicating the loss of long-range crystalline order during solvent removal. Notably, PXRD of activated Zr-MOCs was partially restored to the original profile after soaking in N,N-dimethylacetamide (DMA). This reversible structural change suggested that the tetrahedral cages remained structurally intact, while the activation process mainly disrupted the packing arrangement of the cages [36].

2.2 Solvent-regulated dispersion states of Zr-MOCs

To isolate the intrinsic contribution of cage cavities, it is necessary to establish Zr-MOCs in well-defined dispersion states. In particular, the monodisperse state is required to ensure that individual cages are accessible and separation behavior is governed predominantly by intrinsic cage cavities rather than extrinsic voids arising from cage association. Accordingly, the dispersion behavior of Zr-MOCs was systematically examined in a series of organic solvents with distinct coordinating abilities and boiling points, including DMA, acetonitrile (ACN), methanol (MeOH), and dimethyl sulfoxide (DMSO).

The SEM images and PXRD patterns confirmed that Zr-MOCs

maintained their crystalline morphologies and long-range order in both DMA and ACN solvents, indicating their structural integrity under these conditions (Figs. S2 and S6 in the ESM). Although the diffraction peaks of Zr-MOC-BBC after ACN treatment displayed some variations, the preserved crystal shapes and diffraction features suggested that the cages largely retained their crystalline packing without undergoing disassembly. In contrast, when dispersed in MeOH, the transmission electron microscopy (TEM) images revealed that the crystalline Zr-MOCs underwent partial disassembly, exhibiting irregular aggregates with different shapes and sizes (Fig. 3(a) and Fig. S7 in the ESM). This phenomenon suggested the formation of oligomeric dispersion states. Dynamic light scattering (DLS) measurements further showed broad size distributions ranging from tens to hundreds of nanometers (Fig. 3(b)), indicating the existence of heterogeneous oligomeric assemblies. The dominant particle sizes of oligomeric Zr-MOC-BTB, Zr-MOC-BTE, and Zr-MOC-BBC, as determined from number-based DLS distributions, were 44.05, 126.13, and 59.20 nm, respectively. The broad distributions and absence of discrete size populations reflect a metastable state in which cages partially dissociated but remained associated through residual coordination or secondary interactions. By comparison, no obvious aggregated particles were observed for the DMSO-treated MOCs under comparable TEM characterization conditions (Fig. S8 in the ESM), supporting the absence of oligomeric assemblies in DMSO.

Notably, the high-resolution TEM (HRTEM) images of Zr-MOCs dispersed in DMSO revealed predominantly monodisperse cage particles (Fig. 3(c) and Figs. S9–S11 in the ESM), where the black dots correspond to individual and well-resolved discrete cages. No apparent aggregation or extended assemblies were observed, indicating the high dispersion quality in this solvent. Statistical analysis showed that the average diameters of Zr-MOC-BTB, Zr-MOC-BTE, and Zr-MOC-BBC were 1.78 ± 0.13, 2.71 ± 0.51, and 2.94 ± 0.41 nm, respectively. The relatively narrow size deviations further supported the uniformity of the individual cage structures. DLS profiles also confirmed the monodisperse nature of Zr-MOCs in DMSO (Fig. 3(d)). The number-based DLS distributions exhibited dominant peaks centered at 4.54 nm for Zr-MOC-BTB and Zr-MOC-BTE, and 5.28 nm for Zr-MOC-BBC. The larger hydrodynamic diameters compared to HRTEM results may be reasonably attributed to the presence of solvation shells and the dynamic coordination environment surrounding the cages in solution [37]. The absence of secondary peaks in the DLS profiles further excluded the formation of significant oligomeric aggregates under these conditions. High-angle annular dark-field (HAADF) images further corroborated the predominance of isolated cage entities in DMSO (Fig. S12 in the ESM). In addition, the ^{1}H-nuclear magnetic resonance (^{1}H-NMR) spectra of Zr-MOCs in DMSO-d_6 exhibited simple and well-resolved signals with a single set of ligand proton resonances (Figs. S13–S15 in the ESM), indicating uniform chemical environments and supporting the formation of discrete and highly symmetric coordination cages.

The distinct dispersion states can be rationalized by solvent-cage interactions, evaporation kinetics, and structural reorganization

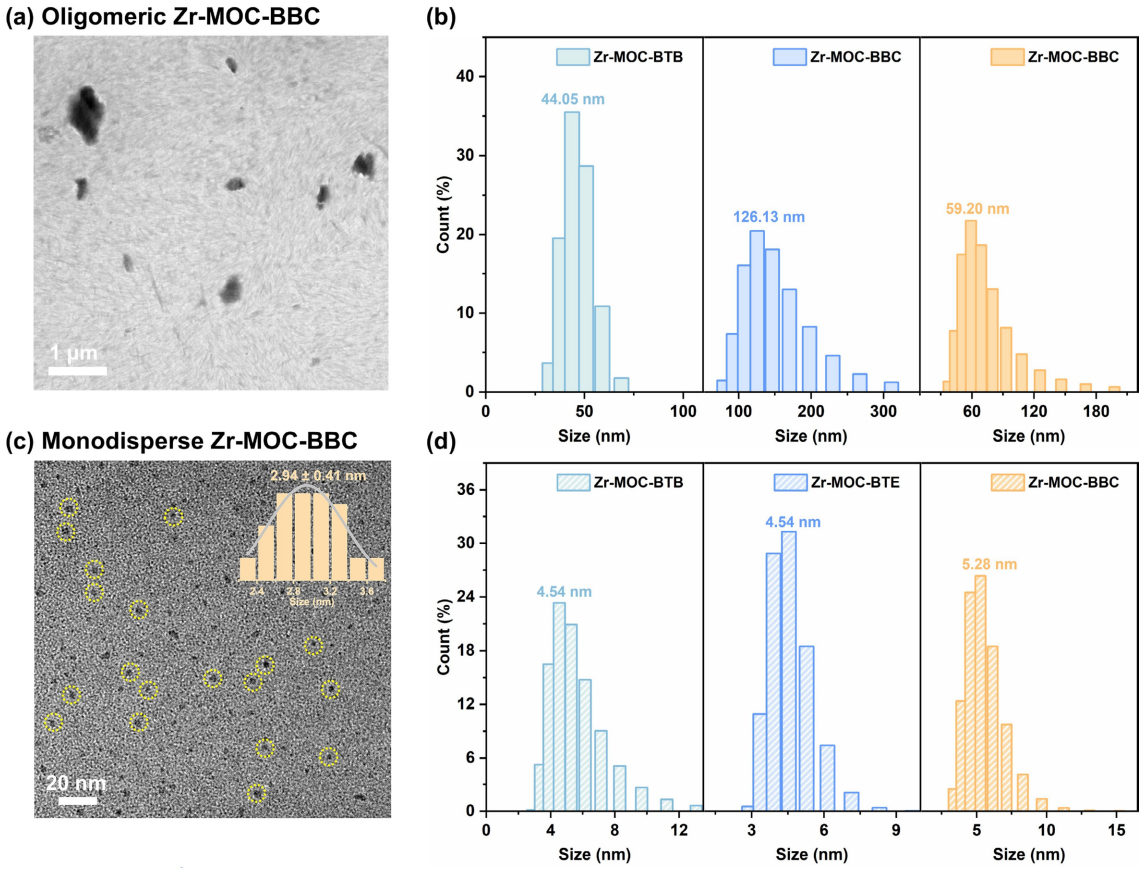


Figure 3 (a) The TEM image of oligomeric Zr-MOC-BBC in MeOH. (b) The DLS plots of oligomeric Zr-MOCs in MeOH. The dominant particle sizes of oligomeric Zr-MOC-BTB, Zr-MOC-BTE, and Zr-MOC-BBC were 44.05, 126.13, and 59.20 nm, respectively. (c) The HRTEM image of monodisperse Zr-MOC-BBC in DMSO. (d) The DLS plots of monodisperse Zr-MOCs in DMSO. The yellow areas had circled several monodisperse cages as a representation. The average sizes of monodisperse Zr-MOC-BTB, Zr-MOC-BTE, and Zr-MOC-BBC were 4.54, 4.54, and 5.28 nm, respectively.

dynamics [38–40]. In general, solvents with higher donor numbers (DNs) exhibit stronger coordination ability toward exposed Zr sites, which can more effectively suppress inter-cage association during solvent removal. Among the solvents investigated, DMSO (DN = 29.8), with its strong coordination ability toward metal centers and a high boiling point, effectively stabilizes the external coordination sphere of the cages [41, 42]. This persistent coordination during slow solvent removal suppresses inter-cage interactions and kinetically traps the system in a monodisperse state composed of discrete molecular species. In contrast, MeOH (DN = 19) exhibits weaker and more dynamic coordination, together with rapid evaporation, than DMSO, leading to insufficient stabilization of exposed coordination sites during solvent removal [43]. This promotes partial cage–cage association, resulting in kinetically trapped oligomeric assemblies. For ACN (DN = 14.1), its weak coordination to Zr centers does not effectively stabilize the cages, while its moderate evaporation rate allows sufficient molecular mobility during solvent removal, enabling the cages to reorganize into thermodynamically favored crystalline packing. For DMA (DN = 27.8), although its coordination strength is comparable to that of DMSO, the amide coordination (C=O) is generally more labile and dynamically exchangeable [44]. This contrasts with the stronger and more persistent coordination of DMSO (S=O), and may allow continued structural reorganization during solvent removal, thereby driving the system toward crystalline packing rather than kinetically trapped monodisperse states. Therefore, these multi-technique characterizations highlight that the dispersion state of Zr-MOCs is not governed solely by solvent polarity, but rather by the coupled effects of coordination strength, solvent removal rate, and coordination dynamics. This interplay enables access to crystalline, oligomeric, or monodisperse cage states. Among the solvents investigated, DMSO uniquely stabilized the cages as discrete entities in solution, thereby providing a well-defined platform for evaluating intrinsic cavity contributions to chromatographic behavior.

2.3 Dispersion state as a prerequisite for efficient Zr-MOC-based separations

Based on the solvent-regulated dispersion behaviors established above, the chromatographic separation performance of Zr-MOCs in different dispersion states was systematically evaluated. All Zr-MOCs were dynamically coated onto capillary columns and thermally aged at 200 °C under N_2 atmosphere (see the ESM for details) [45]. By selecting ACN, MeOH, and DMSO as coating solvents, Zr-MOCs were introduced into the columns, respectively. Notably, due to the large crystal size formed by Zr-MOC-BTB and Zr-MOC-BTE in ACN, only Zr-MOC-BBC can be successfully coated in its crystalline form. Cross-sectional SEM images confirmed that microcrystalline Zr-MOC-BBC was immobilized on the inner wall of the capillary column without significant changes in morphology and particle size (Fig. S16 in the ESM), indicating the structural integrity during the coating process. The separation performance of the 7 columns was then assessed using various analytes, including alkane isomers, substituted benzene isomers, and alkane/cycloalkane/alkene mixtures (Figs. 4(a)–4(c) and Figs. S17–S25 in the ESM), with the corresponding separation resolution (R_s) values summarized in Tables S3–S5 in the ESM.

The crystalline Zr-MOC-BBC-coated column exhibited negligible separation capability (Fig. S17 in the ESM). Given the tetrahedral architecture of the cages, which provides accessible metal sites, confined cavities at the micrometer scale, and ligands capable of hydrophobic interactions, the MOCs themselves were expected to possess intrinsic isomer separation capability. Thus, this poor performance could be attributed to large particle size and the dominance of microcrystalline packing [46], in which intrinsic cage cavities were largely embedded within extended assemblies. Under such conditions, analyte transport was governed primarily by interparticle boundaries rather than well-defined internal pore environments. When Zr-MOC-BBC was introduced in an oligomeric dispersion state using MeOH as the coating solvent, a moderate improvement in separation performance was observed

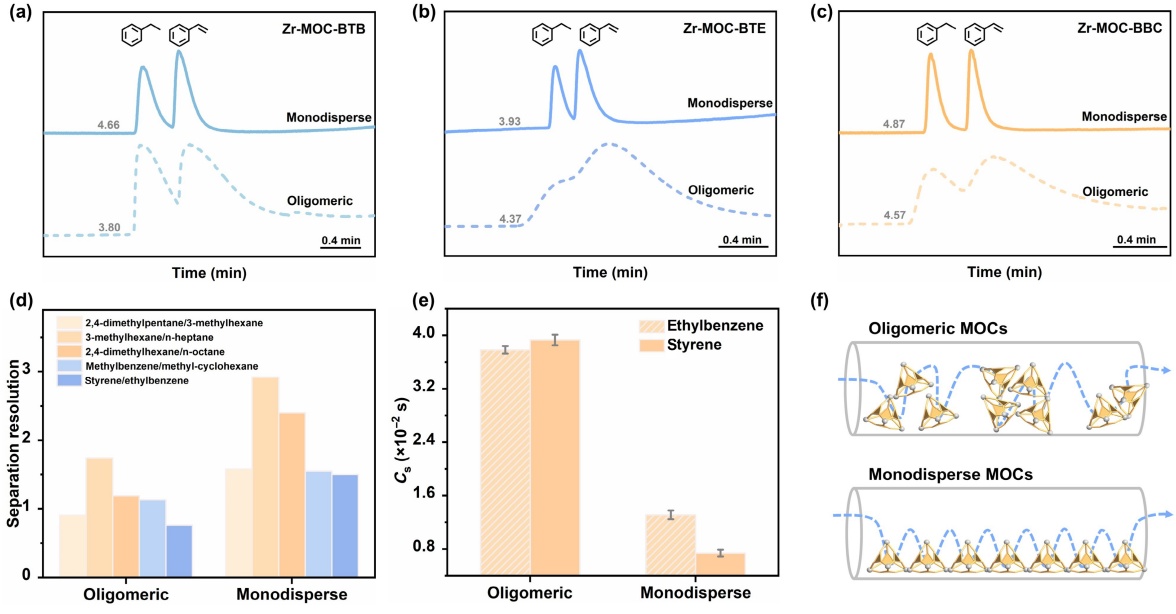


Figure 4 ((a)–(c)) Gas chromatograms for the separation of ethylbenzene/styrene on (a) Zr-MOC-BTB, (b) Zr-MOC-BTE, and (c) Zr-MOC-BBC columns with monodisperse and oligomeric states, respectively. (d) Separation resolution of various analytes on the monodisperse and oligomeric Zr-MOC-BBC columns. (e) The calculated C_s values of ethylbenzene and styrene on the monodisperse and oligomeric Zr-MOC-BBC columns. (f) Schematic illustration of analytes diffusion in oligomeric and monodisperse Zr-MOCs.

(Fig. S18 in the ESM). However, pronounced peak broadening and peak tailing persisted, leading to overall low resolution across all analytes. These chromatographic features suggested that although oligomeric assemblies were less densely packed than crystalline ones, they still generated heterogeneous and inefficient transport pathways. Irregular inter-cage voids and partial cage association likely created tortuous diffusion routes and spatially nonuniform confinement environments, hindering efficient mass transfer under fast GC flow conditions [47]. In contrast, the column coated with monodisperse Zr-MOC-BBC achieved markedly enhanced separation performance (Fig. 4 and Fig. S19 in the ESM). Notably, baseline separation of 2,4-dimethylhexane/n-octane and ethylbenzene/styrene was achieved, with R_s values of 2.4 and 1.5, respectively (Fig. 4(d)). Importantly, the same dispersion-dependent trend was also observed for Zr-MC-BTE and Zr-MOC-BBC (Figs. 4(a) and 4(b)), where monodisperse cages consistently outperformed their oligomeric counterparts. These results established a performance hierarchy among the different dispersion states, with crystalline and oligomeric forms being inferior to the monodisperse state, demonstrating that achieving monodisperse dispersion is the prerequisite for realizing the intrinsic separation potential of MOC-based stationary phases.

To rationalize the dispersion-dependent separation behavior, kinetic diffusion and thermodynamic adsorption analyses were implemented using ethylbenzene and styrene as probe analytes (Figs. S26–S30 in the ESM). Given the consistent trend across all systems, Zr-MOC-BBC was selected as the representative model for mechanistic analysis. The mass transfer resistance (C_s), calculated from the Golay plots, was substantially higher for the oligomeric Zr-MOC-BBC column compared with the monodisperse counterpart (Fig. 4(e)). For example, the C_s value for styrene decreased from $(3.93 \pm 0.08) \times 10^{-2}$ s in the oligomeric state to $(0.74 \pm 0.05) \times 10^{-2}$ s in the monodisperse state (Table S6 in the ESM), corresponding to an approximately fivefold decrease in diffusion resistance. Correspondingly, the diffusion coefficient in the stationary phase (D_s) for styrene was $(1.52 \pm 0.04) \times 10^{-17}$ m^2/s in the oligomeric Zr-MOC-BBC column, smaller than that in the monodisperse Zr-MOC-BBC column ($(8.59 \pm 0.84) \times 10^{-17}$ m^2/s). This difference reflected the disordered and tortuous diffusion pathways associated with oligomeric assemblies, whereas monodisperse cages provided more uniform and accessible environments for analyte diffusion (Fig. 4(f)). Meanwhile, the adsorption enthalpy (ΔH) values derived from van't Hoff plots were nearly identical for oligomeric and monodisperse Zr-MOC-BBC columns (Fig. S29 in the ESM), indicating that the dispersion state exerted a minor influence on the intrinsic host–guest interaction strength. These observations suggested that the improvement in separation performance upon achieving monodisperse dispersion originated predominantly from kinetic factors rather than thermodynamic effects. By minimizing diffusion resistance and eliminating extrinsic transport heterogeneity, monodisperse Zr-MOCs enabled more efficient utilization of their internal cage environments, thereby translating molecular-scale porosity into macroscopic chromatographic separation performance.

2.4 Cavity architecture as an intrinsic determinant of separation performance in monodisperse Zr-MOCs

Having established the monodisperse state as the necessary condition for accessing intrinsic cage effects, we next investigated how cavity architecture influences separation performance under identical dispersion conditions. To exclude contributions from inter-cage association, all comparisons were conducted using monodisperse Zr-MOCs stationary phases prepared with DMSO as the coating solvent (Fig. 5). Among the three monodisperse Zr-MOCs, Zr-MOC-BBC exhibited the highest separation performance, followed by Zr-MOC-BTE, while Zr-MOC-BTB showed the weakest separation ability (Figs. 5(a)–5(c)). For instance, the Zr-MOC-BTB column failed to separate 1,2,4-trichlorobenzene and 1,2,3-trichlorobenzene, whereas partial separation was achieved on the Zr-MOC-BTE column, and baseline separation was obtained on the Zr-MOC-BBC column. This progressive enhancement indicated that enlarged cavity windows increased the separation selectivity, allowing subtle steric variations to be amplified into measurable chromatographic discrimination when extrinsic void effects were eliminated. A similar cavity-dependent trend was also observed for separating alkane isomers, where the Zr-MOC-BBC column outperformed the other columns, demonstrating sharper peaks with minimal tailing and higher resolution (Fig. 5(d)). The R_s of 2,2-dimethylbutane/n-hexane was 3.9 on the Zr-MOC-BBC column, larger than that on Zr-MOC-BTB (R_s = 2.4) and Zr-MOC-BTE (R_s = 2.8) columns. For further comparison, a blank capillary column without MOC coating was evaluated (Fig. S24 in the ESM). In contrast to the MOC-coated columns, the uncoated column exhibited negligible separation capacity, with analytes eluting close to the air peak, indicative of minimal interaction and poor resolution. This result confirmed that effective chromatographic discrimination arose from the presence of MOC stationary phases, and that the observed performance differences originated from variations in intrinsic cavity architecture rather than from the underlying column substrate. Furthermore, the monodisperse Zr-MOC-BBC column demonstrated good repeatability, maintaining consistent separation of ethylbenzene and styrene over six consecutive runs (Fig. S25 in the ESM).

To further correlate cavity architecture with chromatographic behavior, kinetic and thermodynamic parameters were evaluated using n-hexane as the target (Figs. S27 and S30 in the ESM). The C_s values of n-hexane decreased systematically from Zr-MOC-BTB ($(9.62 \pm 0.28) \times 10^{-2}$ s) to Zr-MOC-BTE ($(6.43 \pm 0.19) \times 10^{-2}$ s) and Zr-MOC-BBC ($(3.75 \pm 0.18) \times 10^{-2}$ s), indicating progressively facilitated mass transport as the window and cavity dimensions increased (Fig. 5(e) and Table S7 in the ESM). Larger cage windows reduced the steric barrier for analyte entry, while expanded cavities alleviated diffusional crowding within the cage interior, collectively lowering the overall mass-transfer resistance [48, 49]. Correspondingly, the D_s values increased from Zr-MOC-BTB ($(5.59 \pm 0.23) \times 10^{-18}$ m^2/s) to Zr-MOC-BTE ($(7.90 \pm 0.33) \times 10^{-18}$ m^2/s) and Zr-MOC-BBC ($(15.51 \pm 1.06) \times 10^{-18}$ m^2/s). The diffusion coefficient was 5–6 orders of magnitude lower than that of analogous molecules in framework materials. We attributed this difference to the distinct diffusion mode in cage-based systems, where transport was dominated by barrier-limited hopping and prolonged residence within confined cavities rather than continuous diffusion, leading to orders-of-magnitude lower effective diffusivity. Consistent with the diffusion trend, the column efficiency exhibited a clear dependence on cavity architecture under monodisperse conditions. Using n-hexane as the probe molecule, the Zr-MOC-BBC column achieved the highest efficiency of 658 plates/m (Fig. S28 in the ESM), followed by Zr-MOC-BTE (627 plates/m) and Zr-MOC-BTB (428 plates/m). This result

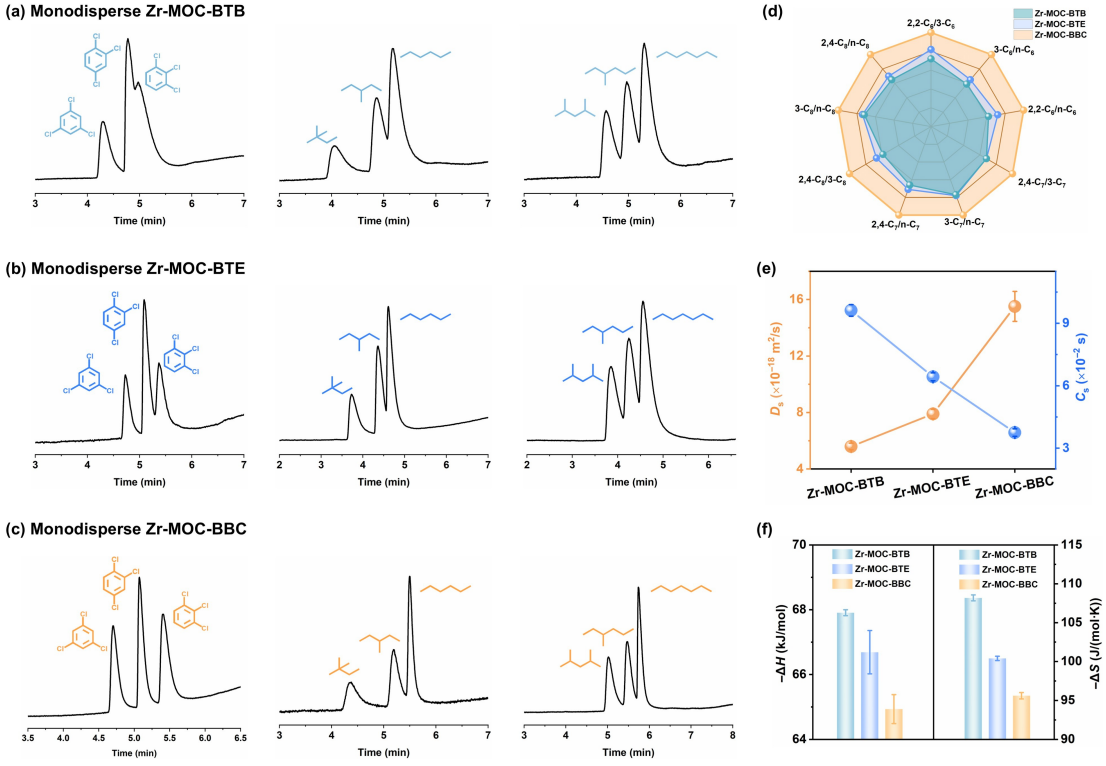


Figure 5 ((a)–(c)) Gas chromatograms of trichlorobenzene isomers, C_6H_{14} isomers, and C_7H16 isomers separated on (a) the monodisperse Zr-MOC-BTB, (b) monodisperse Zr-MOC-BTE, and (c) monodisperse Zr-MOC-BBC coated column (15 m long × 0.25 mm i.d.). (d) Separation resolution of C_6H_{14}, C_7H_{16}, and C_8H_{18} isomers on the monodisperse Zr-MOC-BTB, Zr-MOC-BTE, and Zr-MOC-BBC coated columns. 2,2-C_6, 3-C_6, and n-C_6 represent 2,2-dimethylbutane, 3-methylpentane, and n-hexane, respectively. 2,4-C_7, 3-C_7, and n-C_7 represent 2,4-dimethylpentane, 3-methylhexane, and n-heptane, respectively. 2,4-C_8, 3-C_8, and n-C_8 represent 2,4-dimethylhexane, 3-methylheptane, and n-octane, respectively. (e) The calculated D_s and C_s values and (f) the calculated ΔH and ΔS values of n-hexane on monodisperse Zr-MOC-BTB, Zr-MOC-BTE, and Zr-MOC-BBC coated columns.

reflected the cumulative impact of reduced mass-transfer resistance on chromatographic peak broadening. Nevertheless, the column efficiencies remained lower than those typically reported for framework-based porous stationary phases such as MOFs, which was consistent with the substantially lower diffusivity arising from the discontinuous diffusion pathways in discrete cage systems.

Thermodynamic analysis revealed the negative Gibbs free energy (ΔG) values across all Zr-MOCs, implying the spontaneous transfer of analytes from the mobile phase to the stationary phase [50, 51]. Besides, ΔG values became more favorable with increasing cavity size, decreasing from −16.65 ± 0.31 kJ/mol for Zr-MOC-BTB to −19.38 ± 0.82 kJ/mol for Zr-MOC-BBC, in agreement with the observed enhancement in separation efficiency. Deconvolution of the free energy term revealed distinct and systematic trends in the enthalpic and entropic contributions. As the cavity size increased, the $-\Delta H$ values decreased from 67.91 ± 0.10 kJ/mol for Zr-MOC-BTB to 66.68 ± 0.66 kJ/mol for Zr-MOC-BTE and further to 64.96 ± 0.44 kJ/mol for Zr-MOC-BBC (Fig. 5(f) and Table S8 in the ESM). This gradual attenuation reflected a reduction in confinement-induced host–guest interactions as the cage interior expanded. Smaller cages imposed stronger spatial confinement, which intensified interactions through closer contact between the analyte and the cage interior, whereas enlarged cavities moderated the interaction strength. More pronounced differences were observed in the adsorption entropy (ΔS), highlighting the critical role of cavity size in governing the configurational freedom of adsorbed molecules. Specifically, the $-\Delta S$ values decreased from 108.18 ± 0.38 J/(mol·K) for Zr-MOC-BTB to 100.41 ± 0.27 J/(mol·K) for Zr-MOC-BTE and further to 95.61 ± 0.41 J/(mol·K) for Zr-MOC-BBC (Fig. 5(f)). The substantially less negative value for larger cages indicated a significantly reduced entropy penalty upon adsorption, arising from alleviated restrictions on molecular orientation, translation, and internal degrees of freedom within the expanded cage cavities.

These results demonstrated that optimal separation performance in monodisperse Zr-MOCs arose from a cooperative balance between mass-transfer resistance and thermodynamic host–guest interactions. Enlarging the cage cavity simultaneously alleviated diffusion resistance and reduced the entropic penalty associated with analyte confinement, while maintaining sufficient host–guest interactions for effective retention. With this balanced regime, monodisperse Zr-MOC-BBC efficiently converted its intrinsic cavity architecture into chromatographic performance. Besides, this synergy between moderated confinement and facilitated mass transport enabled Zr-MOC-BBC to achieve higher resolution and column efficiency among the monodisperse Zr-MOCs studied.

3 Conclusions

In summary, Zr-MOC-BTB, Zr-MOC-BTE, and Zr-MOC-BBC with identical topology but systematically varied cavity size were constructed and evaluated as GC stationary phases. Their dispersion behavior was found to be strongly dependent on the solvent, giving rise to crystalline, oligomeric, or monodisperse states. By identifying conditions that stabilize monodisperse cages, we were able to minimize inter-cage packing effects and directly probe the role of intrinsic cage cavities in separation. Under

monodisperse conditions, the separation performance of MOCs was significantly improved compared to aggregated states. Furthermore, among the monodisperse MOCs, Zr-MOC-BBC with increased cavity size exhibited improved separation resolution, indicating that intrinsic geometric parameters play a key role once dispersion effects are controlled. These results highlight the importance of dispersion state in determining the performance of MOC-based stationary phases and provide useful guidance for their future design.

Electronic Supplementary Material: Supplementary material (the experimental section, MOF characterization, and GC separation chromatogram) is available in the online version of this article at https://doi.org/10.26599/NR.2026.94908924.

Data availability

All data needed to support the conclusions in the paper are presented in the manuscript and the Electronic Supplementary Material. Additional data related to this paper may be requested from the corresponding author upon request.

Acknowledgements

This work was supported by the National Natural Science Foundation of China (Nos. 22474059 and 22374077), the Science and Technology Major Project of Jiangsu Province (No. BG2025045), and the Priority Academic Program Development of Jiangsu Higher Education Institutions. This work was carried out with the support of BL17B1 at the Shanghai Synchrotron Radiation Facility (proposal 2023-NFPS-PT-500772).

Declaration of competing interest

All the contributing authors report no conflict of interests in this work.

Author contribution statement

S.-S. M.: Data curation, project administration, validation, writing manuscript, experimental design, and collecting data. C.-Y. R.: Data curation, experimental design, and collecting data. M. X.: Project administration, funding acquisition, and revising manuscript. Z.-Y. G.: Project administration and funding acquisition. All the authors have approved the final manuscript.

Use of AI statement

None.

References

[1] Lee, S.; Jeong, H.; Nam, D.; Lah, M. S.; Choe, W. The rise of metal-organic polyhedra. *Chem. Soc. Rev.* **2021**, *50*, 528–555.

[2] Yoshizawa, M.; Klosterman, J. K.; Fujita, M. Functional molecular flasks: New properties and reactions within discrete, self-assembled hosts. *Angew. Chem., Int. Ed.* **2009**, *48*, 3418–3438.

[3] Liu, J. J.; Wang, Z. F.; Cheng, P.; Zaworotko, M. J.; Chen, Y.; Zhang, Z. J. Post-synthetic modifications of metal-organic cages. *Nat. Rev. Chem.* **2022**, *6*, 339–356.

[4] Liu, Y. W.; Li, G.; Zhang, X.; Du, Z. L.; Zhang, T. T.; Zhang, Y. Y.; Lavendomme, R.; Gao, E. Q.; Zhang, D. W. A hexadecacationic metal-organic cage for anchoring sulfonates: High-order binding of di- and trisulfonates and high-performance removal of perfluorosulfonates from water. *Adv. Sci.* **2026**, *13*, e15258.

[5] Zhu, C. F.; Yang, K. K.; Wang, H. Z.; Fang, Y.; Feng, L.; Zhang, J. Q.; Xiao, Z. F.; Wu, X.; Li, Y. G.; Fu, Y. M. et al. Enantioseparation in hierarchically porous assemblies of homochiral cages. *ACS Cent. Sci.* **2022**, *8*, 562–570.

[6] Liu, B. H.; Peng, S. P.; Wang, H.; Liu, X. X.; Peng, Y. W.; Yuan, G. Z.; Xia, Q. C. Ultrathin nanosheets formed by metal-organic cages connected via hydrogen bonds. *J. Am. Chem. Soc.* **2026**, *148*, 1934–1943.

[7] Li, D.; Zhang, J.; Landskron, K.; Liu, T. B. Spontaneous self-assembly of metal-organic cationic nanocages to form monodisperse hollow vesicles in dilute solutions. *J. Am. Chem. Soc.* **2008**, *130*, 4226–4227.

[8] Feng, X. Y.; Liu, X. P.; Gao, F.; Wang, X. K.; Fan, W. D.; Feng, X.; Lu, Y. K.; Yuan, D. Q.; Sun, D. F. Multivariate metal-organic cages for efficient C_2H_2/CO_2 separation. *ACS Mater. Lett.* **2026**, *8*, 284–290.

[9] Xu, Y.; Li, G.; Liang, S. H.; De Leener, G.; Luhmer, M.; Lavendomme, R.; Gao, E. Q.; Zhang, D. W. Engineering cavity and aperture binding sites within a metal-organic cage for up- and down-regulation of catalysis. *Angew. Chem.* **2025**, *137*, e202507981.

[10] Morey, M. N.; Montone, C. M.; Dworzak, M. R.; Yap, G. P. A.; Bloch, E. D. Tunable synthesis of heteroleptic zirconium-based porous coordination cages. *Chem. Sci.* **2024**, *16*, 816–823.

[11] Liu, G. L.; Di Yuan, Y.; Wang, J.; Cheng, Y. D.; Peh, S. B.; Wang, Y. X.; Qian, Y. H.; Dong, J. Q.; Yuan, D. Q.; Zhao, D. Process-tracing study on the postassembly modification of highly stable zirconium metal-organic cages. *J. Am. Chem. Soc.* **2018**, *140*, 6231–6234.

[12] Yadav, A. K.; Gładysiak, A.; Wolpert, E. H.; Ganose, A. M.; Samel-Garloff, B.; Koley, D.; Jelfs, K. E.; Stylianou, K. C. Solvatomorphic diversity dictates the stability and solubility of metal-organic polyhedra. *Chem. Sci.* **2025**, *16*, 2589–2599.

[13] Fan, W. D.; Peh, S. B.; Zhang, Z. Q.; Yuan, H. Y.; Yang, Z. Q.; Wang, Y. X.; Chai, K. G.; Sun, D. F.; Zhao, D. Tetrazole-functionalized zirconium metal-organic cages for efficient C_2H_2/C_2H_4 and C_2H_2/CO_2 separations. *Angew. Chem., Int. Ed.* **2021**, *60*, 17338–17343.

[14] Qin, L. Z.; Xiong, X. H.; Wang, S. H.; Meng, L. L.; Yan, T. A.; Chen, J.; Zhu, N. X.; Liu, D. H.; Wei, Z. W. A series of functionalized zirconium metal-organic cages for efficient CO_2/N_2 separation. *Inorg. Chem.* **2021**, *60*, 17440–17444.

[15] Zhu, J. L.; Zhang, D. W.; Ronson, T. K.; Wang, W. J.; Xu, L.; Yang, H. B.; Nitschke, J. R. A cavity-tailored metal-organic cage entraps gases selectively in solution and the amorphous solid state. *Angew. Chem., Int. Ed.* **2021**, *60*, 11789–11792.

[16] Qi, X. J.; Zhong, R. L.; Chen, M. M.; Sun, C. Y.; You, S. Q.; Gu, J. X.; Shan, G. G.; Cui, D. X.; Wang, X. L.; Su, Z. M. Single metal-organic cage decorated with an Ir(III) complex for CO_2 photoreduction. *ACS Catal.* **2021**, *11*, 7241–7248.

[17] Liu, X. L.; Wang, X. R.; Bavykina, A. V.; Chu, L. Y.; Shan, M. X.; Sabetghadam, A.; Miro, H.; Kapteijn, F.; Gascon, J. Molecular-scale hybrid membranes derived from metal-organic polyhedra for gas separation. *ACS Appl. Mater. Interfaces* **2018**, *10*, 21381–21389.

[18] Longo, M.; Mobili, R.; Monteleone, M.; La Cognata, S.; Fuoco, A.; Esposito, E.; Boiocchi, M.; Milanese, C.; Armentano, D.; Hajivand, P. et al. Metal-organic cages in polyimide and polyetheretherketone thin film composite mixed matrix membranes for gas separation. *J. Membr. Sci.* **2025**, *714*, 123391.

[19] Zhang, J. H.; Xie, S. M.; Zi, M.; Yuan, L. M. Recent advances of application of porous molecular cages for enantioselective recognition and separation. *J. Sep. Sci.* **2020**, *43*, 134–149.

[20] Zhang, J. H.; Liang, R. X.; Huang, B.; Yu, L. Q.; Chen, J.; Wang, B. J.; Xie, S. M.; Yuan, L. M. Preparation of a homochiral metal-organic cage and its bonded silicas for efficient enantioseparation in high-performance liquid chromatography and gas chromatography. *Chin. Chem. Lett.* **2026**, *37*, 111146.

[21] Xie, S. M.; Fu, N.; Li, L.; Yuan, B. Y.; Zhang, J. H.; Li, Y. X.; Yuan, L. M. Homochiral metal-organic cage for gas chromatographic separations. *Anal. Chem.* **2018**, *90*, 9182–9188.
[22] Liu, C. F.; Chen, J. K.; Guo, P.; Lu, Y. R.; Yang, Y. P.; Wang, B. J.; Zhang, J. H.; Xie, S. M.; Yuan, L. M. A chiral metal-organic cage $[Fe_4L_6](ClO_4)_8$ used for capillary gas chromatographic separations. *Anal. Chim. Acta* **2022**, *1224*, 340197.
[23] Zhu, Y. L.; Yang, Y. P.; Ma, A. X.; Ran, X. Y.; Liu, C.; Wang, B. J.; Zhang, J. H.; Xie, S. M.; Yuan, L. M. A chiral metal-organic polyhedron used as stationary phase for gas chromatographic separations. *Microchem. J.* **2024**, *200*, 110331.
[24] Tang, B.; Zhang, X.; Geng, L. N.; Sun, L. Q.; Luo, A. Q. A chiral metal-organic cage used as the stationary phase for gas chromatography separations. *J. Chromatogr. A* **2021**, *1636*, 461792.
[25] Luo, Z. H.; Zhu, Y. L.; Ran, X. Y.; Ma, A. X.; Zhang, Y.; Zhou, H. M.; Wang, B. J.; Zhang, J. H.; Xie, S. M.; Yuan, L. M. Subcomponent self-assembly construction of tetrahedral cage $Fe^{II}_4L_4$ for high-resolution gas chromatographic separation. *Talanta* **2024**, *277*, 126388.
[26] Meng, S. S.; Wei, H. Y.; Yang, H.; Zhang, J.; Xu, M.; Gu, Z. Y. Modulating the cavity micro-environments of Fe-MOFs for high-performance gas chromatographic separations. *Talanta* **2025**, *283*, 127100.
[27] Zeng, C.; Jiang, H. T.; Xu, M.; Gu, Z. Y. Stabilizing an scu-topology Zr-MOF via linker installation for enhanced gas chromatographic separation. *Talanta* **2026**, *303*, 129469.
[28] Zhu, Z. L.; Xiao, J. F.; Zhang, M.; Huang, Y. Q.; Yuan, S. J. Precision pore engineering via fit-topology assembly in a Zn-porphyrin MOF for selective C_2H_2 capture. *Chem. Sci.* **2025**, *16*, 22638–22646.
[29] Zhu, Z. L.; Xiao, J. F.; Li, R. Y.; Huang, Y. Q.; Yuan, S. J. Dual-ligand-engineered ultramicroporous porphyrinic MOF for efficient C_2H_6/C_2H_4 and C_2H_2/CO_2 separations. *Small* **2026**, *22*, e73567.
[30] Yang, Y. J.; Zhang, Y. Y.; Li, P. F.; Sun, B. B.; Zha, Y.; Peng, F.; Gan, L.; Huang, H. L.; Yang, H. J. Isomeric nonpolar amino acid-derived metal-organic frameworks for xenon/krypton separation. *Angew. Chem., Int. Ed.* **2026**, *65*, e5896266.
[31] Liu, G. L.; Ju, Z. F.; Yuan, D. Q.; Hong, M. C. *In situ* construction of a coordination zirconocene tetrahedron. *Inorg. Chem.* **2013**, *52*, 13815–13817.
[32] Zhang, G.; Presly, O.; White, F.; Oppel, I. M.; Mastalerz, M. A permanent mesoporous organic cage with an exceptionally high surface area. *Angew. Chem., Int. Ed.* **2014**, *53*, 1516–1520.
[33] Welgama, H. K.; Avasthi, A.; Cook, T. R. Metal-organic polyhedra and metal-organic frameworks: Understanding how discrete versus extended structure impacts surface areas and pore size distributions. *Chem. Mater.* **2024**, *36*, 4185–4195.
[34] Yi, M. H.; Cheng, Y. P.; Wang, Z. Y.; Wang, C. H.; Hu, B.; He, X. X. Effect of particle size and adsorption equilibrium time on pore structure characterization in low pressure N_2 adsorption of coal: An experimental study. *Adv. Powder Technol.* **2020**, *31*, 4275–4281.
[35] Doñagueda Suso, B.; Legrand, A.; Weetman, C.; Kennedy, A. R.; Fletcher, A. J.; Furukawa, S.; Craig, G. A. Porous metal-organic cages based on rigid bicyclo[2.2.2]oct-7-ene type ligands: Synthesis, structure, and gas uptake properties. *Chem.—Eur. J.* **2023**, *29*, e202300732.
[36] Nam, D.; Huh, J.; Lee, J.; Kwak, J. H.; Jeong, H. Y.; Choi, K.; Choe, W. Cross-linking Zr-based metal-organic polyhedra via postsynthetic polymerization. *Chem. Sci.* **2017**, *8*, 7765–7771.
[37] Kim, S.; Jee, S.; Choi, K. M.; Shin, D. S. Single-atom Pd catalyst anchored on Zr-based metal-organic polyhedra for Suzuki–Miyaura cross coupling reactions in aqueous media. *Nano Res.* **2021**, *14*, 486–492.
[38] Benchimol, E.; Nguyen, B. N. T.; Ronson, T. K.; Nitschke, J. R. Transformation networks of metal-organic cages controlled by chemical stimuli. *Chem. Soc. Rev.* **2022**, *51*, 5101–5135.
[39] Chen, X.; Li, S. B.; Liu, Z. Y.; Zhang, Y. T. Solvent-directed assembly of Zr-based metal-organic cages for dye adsorption from aqueous solution. *J. Solid State Chem.* **2021**, *296*, 121998.
[40] Miao, L. L.; Zhu, X. J.; Liu, G. X.; Han, X.; Xie, W. P.; Lu, S.; Zhang, L.; Wang, K.; Shi, L. L.; Lu, S. Y. et al. Tunable aggregation-induced fluorescent and pressure-responsive luminescence supramolecular cages achieved by subcomponent self-assembly. *Chin. Chem. Lett.* **2023**, *34*, 107921.
[41] Niu, Z.; Wang, L.; Fang, S.; Lan, P. C.; Aguila, B.; Perman, J.; Ma, J. G.; Cheng, P.; Li, X. P.; Ma, S. Q. Solvent-assisted coordination driven assembly of a supramolecular architecture featuring two types of connectivity from discrete nanocages. *Chem. Sci.* **2019**, *10*, 6661–6665.
[42] Niu, W. X.; Duan, Y. K.; Qing, Z.; Huang, H. J.; Lu, X. M. Shaping gold nanocrystals in dimethyl sulfoxide: Toward trapezohedral and bipyramidal nanocrystals enclosed by {311} facets. *J. Am. Chem. Soc.* **2017**, *139*, 5817–5826.
[43] Caratelli, C.; Hajek, J.; Rogge, S. M. J.; Vandenbrande, S.; Meijer, E. J.; Waroquier, M.; Van Speybroeck, V. Influence of a confined methanol solvent on the reactivity of active sites in UiO-66. *ChemPhysChem* **2018**, *19*, 420–429.
[44] Helm, L.; Merbach, A. E. Inorganic and bioinorganic solvent exchange mechanisms. *Chem. Rev.* **2005**, *105*, 1923–1960.
[45] Qian, H. L.; Yang, C. X.; Yan, X. P. Bottom-up synthesis of chiral covalent organic frameworks and their bound capillaries for chiral separation. *Nat. Commun.* **2016**, *7*, 12104.
[46] Meng, S. S.; Han, T.; Gu, Y. H.; Zeng, C.; Tang, W. Q.; Xu, M.; Gu, Z. Y. Enhancing separation abilities of "low-performance" metal-organic framework stationary phases through size control. *Anal. Chem.* **2022**, *94*, 14251–14256.
[47] Xu, M.; Meng, S. S.; Cai, P. Y.; Tang, W. Q.; Yin, Y. D.; Powell, J. A.; Zhou, H. C.; Gu, Z. Y. Modulating the stacking modes of nanosized metal-organic frameworks by morphology engineering for isomer separation. *Chem. Sci.* **2021**, *12*, 4104–4110.
[48] Gaidimas, M. A.; Son, F. A.; Mian, M. R.; Islamoglu, T.; Farha, O. K. Influence of pore size on hydrocarbon transport in isostructural metal-organic framework crystallites. *ACS Appl. Mater. Interfaces* **2022**, *14*, 47222–47229.
[49] Sun, B. B.; Zeng, C.; Deng, S. Y.; Gu, Y. W.; Gan, L.; Yang, H. J. Adsorption kinetics-driven humidity-resistant C_2H_2/CO_2 separation by a hydrophilic metal-organic framework. *Chem. Mater.* **2025**, *37*, 1154–1159.
[50] Yusuf, K.; Natraj, A.; Li, K.; Ateia, M.; Alothman, Z. A.; Dichtel, W. R. Inverse gas chromatography demonstrates the crystallinity-dependent physicochemical properties of two-dimensional covalent organic framework stationary phases. *Chem. Mater.* **2023**, *35*, 1691–1701.
[51] Natraj, A.; Ji, W.; Xin, J. J.; Castano, I.; Burke, D. W.; Evans, A. M.; Strauss, M. J.; Ateia, M.; Hamachi, L. S.; Gianneschi, N. C. et al. Single-crystalline imine-linked two-dimensional covalent organic frameworks separate benzene and cyclohexane efficiently. *J. Am. Chem. Soc.* **2022**, *144*, 19813–19824.

This is an open access article under the terms of the Creative Commons Attribution 4.0 International License (CC BY 4.0, https://creativecommons.org/licenses/by/4.0/).

© The Author(s) 2026. Published by Tsinghua University Press.